Sea ice concentration retrieval in the Antarctic based on the SSM/I 85.5 GHz polarization

Stefan Kern, Georg Heygster
Institute of Environmental Physics, P.O.Box 33 04 40, D-28334 Bremen, Germany

ABSTRACT. Using data from the 85 GHz channels of the Special Sensor Microwave/Imager (SSM/I) allows a resolution improvement by at least a factor of four if compared to the other channels. Consequently, higher-resolution sea-ice concentration data can be obtained which in turn can be used to improve the results of Numerical Weather Prediction (NWP) and global circulation models. The proposed new sea-ice concentration retrieval algorithm (SEA LION algorithm) uses the polarization at 85 GHz (P). Emission from atmospheric water and scattering at the wind-roughened sea surface (weather effect) decrease P and cause an overestimation of the sea-ice concentration. We quantify the weather effect with a radiative transfer model and atmospheric data obtained from NWP models and the other SSM/I channels, and correct P for this effect. Tie points of open water and sea ice are determined for each month separately from daily gridded 85 GHz SSM/I brightness temperatures. Sea-ice concentrations are calculated with the new algorithm for the entire Southern Ocean for each day of the period 1992–98 with a spatial resolution of $12.5 \times 12.5\,\mathrm{km}^2$. Comparisons of these ice concentrations with Operational Linescan System visible images reveal convincing results concerning the monitoring of coastal polynyas and the break-up of the pack ice in spring. SEA LION sea-ice extents and areas, and comparisons between SEA LION sea-ice concentrations and ship observations, agree with those obtained by the NASA-Team and the Bootstrap algorithms.

1 Introduction

In this paper, we describe and test a new algorithm which exploits the higher spatial resolution of the 85 GHz channels of the spaceborne passive microwave radiometer Special Sensor Microwave/Imager (SSM/I) to retrieve higher resolution daily sea ice concentration data than are currently provided by known algorithms. The SSM/I sensor, first launched in 1987 as part of the Defense Meteorological Satellite Program (DMSP), scans the Earths' surface conically with a constant ground surface incidence angle of 53.1° and is equipped with three channels with both vertical and horizontal polarization at 19.35, 37.0, and 85.5 GHz and one with just vertical polarization at 22.235 GHz (Hollinger and others, 1987). Among others, the Bootstrap algorithm (Comiso and others, 1992) and the NASA-Team algorithm (Cavalieri and others, 1991) are have been used for sea ice concentration retrieval based on the 19 and 37 GHz channels of the SSM/I for many years. However, both algorithms suffer from the large sensor footprint of $69 \times 43\,\mathrm{km}^2$ (19 GHz) and of $37 \times 28\,\mathrm{km}^2$ (37 GHz).
The 85 GHz footprint ($15 \times 13\,\mathrm{km}^2$) allows a much better spatial resolution. Svendsen and others (1987) were the first to use frequencies near 90 GHz for sea ice concentration retrieval. Their results are based on the brightness temperature polarization difference (BTPD) and have been confirmed for clear sky winter (*e. g.* Lomax and others, 1995) and overcast summer conditions (Lubin and others, 1997). We use the normalized brightness temperature polarization difference (NBTPD) (also called polarization) at 85 GHz instead of the BTPD to minimize the influence of a change of the physical temperature of the radiating portion of the sea ice cover. In this study, the other SSM/I channels are not used to retrieve the sea ice concentration.
Sea ice significantly reduces the exchange of sensible and latent heat as well as momentum between oceans and atmospheres (Maykut, 1978). Exact knowledge of these surface fluxes is very important for modeling atmospheric dynamics and thermodynamics with Numerical Weather Prediction (NWP) models. Over sea ice, the quality of the modeled fluxes is determined by surface properties like the sea ice concentration which can be calculated from spaceborne remote sensing data, as well as its thickness and roughness, quantities that are more difficult to estimate from remote sensing data. The spatial resolution of these data covers several orders of magnitude (Synthetic Aperture Radar (SAR): 25 m, SSM/I: > 25 km). Though SAR is an excellent source for detailed information on type and structure of a sea ice cover (Drinkwater, 1998), geophysical parameters calculated from passive microwave data on a hemispherical scale like the SSM/I sea ice concentration are more suitable to NWP models and Global Circulation Models. The following Sections will focus on the basis and on error sources of the presented method. The effects of snow cover and intervening atmosphere, which vary both spatially and temporally, are discussed and accounted for by the use of temporal tie points and a radiative transfer

This work was supported by the European Union, Contract: ENV4-CT97-0415. SSM/I data were provided by the Earth Observing System Distributed Active Archive Center at the NSIDC, University of Colorado, Boulder. Other data were provided by the Antarctic Meteorology Research Centeer (Space Science Engineering Center, Madison, WI), the ECMWF (Reading, UK) and Deutsches Klimarechenzentrum (Hamburg, Germany). We would like to thank C. Haas, C. Garrity, and R. Ramseier for useful discussions. The help of two anonymous referees and the scientific editor R. Massom is gratefully achnowledged.

model, respectively. The algorithm has been used to obtain daily sea ice concentration data for the period 1992–1998 of which some examples will be shown.

2 Method

The basis of the presented SEA LION algorithm is as follows. The brightness temperature T_p emitted at polarization p from a partly sea ice covered area equal to unity with the fractions of sea ice C and open water $1-C$ can be written as

$$T_p = (1-C)\epsilon_{p,w}T_{s,w} + C\epsilon_{p,i}T_{s,i}, \qquad (1)$$

where the emissivities of open water and sea ice at polarization p are given by $\epsilon_{p,w}$ and $\epsilon_{p,i}$, respectively, and $T_{s,w}$ and $T_{s,i}$ denote the temperatures of the sea surface and of the emitting layer of the sea ice, respectively. This approach follows the one of Svendsen and others (1987) omitting multiyear ice since the Antarctic sea ice cover primarily consists of first-year (FY) ice. The NBTPD which is used *e. g.* in the NASA-Team algorithm is defined as

$$P = \frac{T_v - T_h}{T_v + T_h}, \qquad (2)$$

where T_v and T_h are the brightness temperatures at vertical and horizontal polarization, respectively. The NBTPD calculated from ϵ_p measured at 90 GHz in the Weddell Sea (Comiso and others, 1992) is small over sea ice but quite large over open water (see Table 1). Inserting of Equation 1 in Equation 2 yields

$$C = \left(1 + \frac{T_{v,i} + T_{h,i}}{T_{v,w} + T_{h,w}} \frac{P_i - P}{P - P_w}\right)^{-1}, \qquad (3)$$

where the triplets P_w, $T_{v,w}$, $T_{h,w}$ and P_i, $T_{v,i}$, $T_{h,w}$ are the tie points of open water and sea ice, respectively, which we calculate prior to the retrieval of C. Since Equation 3 is valid for surface measurements only, the usage of SSM/I data requires to consider the atmosperic influence (see Section 2.2).

2.1 Tie points

The wavelength at 85 GHz is small if compared to the other SSM/I channels. This has two consequences. At first, sea ice becomes radiometrically opaque at a smaller thickness (Grenfell and others, 1998). Secondly, emission and, more important, scattering in the snow provide a more significant contribution to the radiometric signal of snow covered sea ice (Grenfell and others, 1994, 1998) and may smooth different signals caused by different sea ice types. However, the snow cover properties, *e. g.* the liquid water content, the grain size and the density, show a large spatial and temporal variability (Massom and others, 1998; Sturm and others, 1998) and change within one day as well as throughout the year due to thermodynamic snow metamorphosis and precipitation (Garrity, 1992; Massom and others, 1998; Sturm and others, 1998). Antarctic sea ice is covered by snow most of the year (Worby and Massom, 1995; Massom and others, 1998; Sturm and others, 1998).

Taking this into account, the emissivities, which are given in Table 1 and which were taken in the Weddell Sea in winter and spring only (Comiso and others, 1992), are not representative for the sea ice conditions of the entire Antarctic all the year round. Instead, considering this lack of information and the highly varying snow properties, we decided to derive monthly sea ice tie points as follows. Monthly averages of the NBTPD, $\bar{P}$, and the temporal variability (variance) σ_P^2 are calculated for each pixel using the NSIDC daily gridded SSM/I brightness temperatures. The averages of P (not shown) allow to separate sea ice ($\bar{P} < 0.05$) from open water ($\bar{P} \approx 0.12$). Over open water, $\bar{P}$ is significantly smaller than *in situ* measurements of P (Table 1) because of the monthly average weather influence which extends also onto the sea ice. The variances of P (not shown) increase towards the marginal ice zone (MIZ), *i. e.* pixel being closer to the MIZ exhibit a larger temporal variability if compared to pack ice pixel. This can be explained by an increasing variability of C and an increase of the direct (atmospheric water) and indirect (precipitation, melt-thaw cycles, flooding) weather influences towards the MIZ. Over polynyas, $\bar{P}$ is smaller and σ_P^2 is larger if compared to other pack ice areas, for C and atmospheric water contents are more variable.

The sea ice tie points $T_{p,i}$ and P_i (Figure 1) are calculated by averaging only values of T_p and P belonging to areas where for the given month $\bar{P} < 0.05$ and $\sigma_P^2 < 25 \times 10^{-6}$ ($\approx \sigma_P < 0.005$, see Table 1). Thus almost all pixels with $C < 100\,\%$ and with a highly variable polarization, either due to changing surface properties or weather conditions or both are excluded. The high limit chosen for $\bar{P}$ ensures that nilas (Table 1) is considered. Open water tie points $T_{p,w}$ and P_w are also calculated for each month separately from NSIDC daily gridded clear sky SSM/I brightness temperatures taken in proximity to the ice edge. Finally, the residual direct weather influences by surface wind and atmospheric water vapor over open water and by atmospheric water over sea ice are quantified and substracted (Section 2.2). Tie points are calculated for all months of the period 1992–98. Monthly sea ice tie points averaged over this period are shown in Figure 1.

2.2 Atmospheric influence

If compared to the Arctic, the atmospheric influence on the SSM/I measurements is much more pronounced in the antarctic sea ice zone due to its proximity to the Southern Ocean, which is a substantial source of atmospheric heat and moisture and a site of significant cyclogenesis (King and Turner, 1997). The increase of the SSM/I brightness temperatures due to emission from atmospheric water (integrated water vapor W and integrated cloud liquid water L) is larger at 85 GHz than at the other SSM/I channels (Ulaby and others, 1981). Though this increase is less significant over most sea ice covered areas for their high surface emissivities, it becomes larger with decreasing surface emissivities *e. g.*

Table 1: Surface emissivities ϵ_p at 90 GHz, v- and h-polarization, measured *in situ* in the Weddell Sea, Antarctica (Comiso and others, 1992), their standard deviations σ_{ϵ_p}, and P and corresponding standard deviations σ_P calculated from these measurements

.

90 GHz	Open water	Gray nilas	Light nilas	Pancake ice	Cold FY ice	Melting FY ice
$\epsilon_v \pm \sigma_{\epsilon_v}$	0.785 ± 0.050	0.922 ± 0.020	0.961 ± 0.024	0.941 ± 0.058	0.954 ± 0.036	0.921 ± 0.039
$\epsilon_h \pm \sigma_{\epsilon_h}$	0.530 ± 0.060	0.841 ± 0.051	0.927 ± 0.018	0.892 ± 0.063	0.919 ± 0.026	0.881 ± 0.027
$P \pm \sigma_P$	0.194 ± 0.024	0.046 ± 0.019	0.018 ± 0.003	0.027 ± 0.004	0.019 ± 0.005	0.022 ± 0.006

over the MIZ (Fuhrhop and others, 1998) and has to be corrected. Figure 1 shows the increase of C due to W and L for a calm icefree sea surface (Salinity: 34 ppt; Surface temperature: 0 °C), calculated from uncorrected 85 GHz SSM/I brightness temperatures with Equation 3. Over open water, C could be 90 % or higher. Over 100 % of cold FY ice (see Table 1) this increase (not shown) is still one tenth of that over open water.

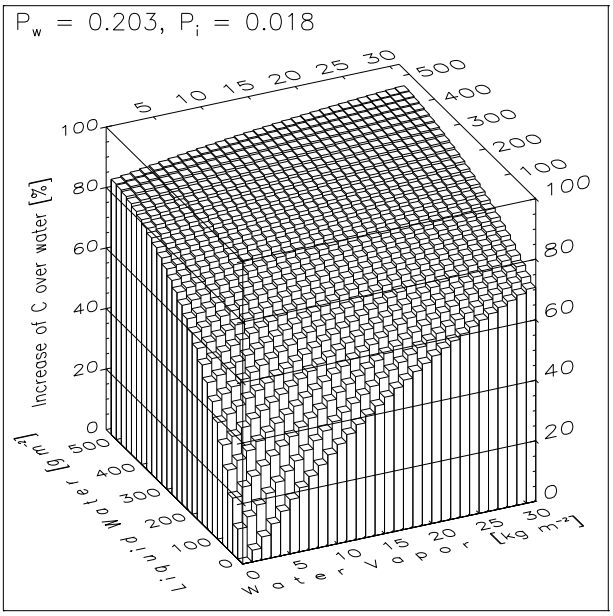

Figure 1: Increase of C due to W and L calculated with Equation 3 from uncorrected 85 GHz SSM/I brightness temperatures over a calm sea surface with C=0 % and P_i and P_w as given in the upper left corner.

In order to quantify the influence caused by W and L, we modeled brightness temperatures with the radiative transfer model MWMOD (MicroWave MODel) (Fuhrhop and others, 1998) for $\epsilon_p = 0.44...0.98$ (stepsize: 0.01) and typical values of W and L. For each ϵ_p a 2-D polynomial fit yields a set of coefficients that allows to substract the quantified atmospheric water influence from the SSM/I brightness temperatures knowing ϵ_p, W and L. The latter are obtained from the low SSM/I frequencies and NWP models. Over sea ice, ϵ_p is estimated from $T_{p,i}$ and monthly average surface temperatures taken from the operational NWP model of the European Centre for Medium range Weather Forecast (ECMWF). Over open water, ϵ_p is altered by the surface wind (Ulaby and others, 1981). In particular, surface wind speeds V larger than $10\,\mathrm{ms}^{-1}$ significantly decrease P at 85 GHz causing again an overestimation of C if neglected. We used MWMOD to calculate sea surface emissivities and to quantify the change of T_p for typical wind speeds. The emissivities are put into a look-up table. For each given V this table provides the correct sea surface emissivity required by the correction of the influence of W and L on T_p. The changes of T_p according to V are substracted from the brightness temperatures after this correction.

2.3 Algorithm

Equation 3 is the basis for SEA LION which iteratively calculates and minimizes the difference between P obtained from the uncorrected NSIDC daily gridded 85 GHz SSM/I brightness temperatures and P obtained from brightness temperatures modeled according to the given atmospheric condition and the retrieved C. The first iteration step is calculating a first-guess sea ice concentration C_{FG} using Equation 3 and uncorrected SSM/I data. In order to prove C_{FG}, brightness temperatures are modeled with MWMOD according to the values of W, L, V and C_{FG}. If P obtained from these modeled brightness temperatures differs from the measured one by less than 0.001 ($\approx$1 % change in C), C_{FG} is taken as the actual sea ice concentration and the iteration is stopped.
Otherwise the weather influence given by W, L and V is quantified and substracted from the SSM/I brightness temperatures. A first-order weather-corrected P is calculated from these reduced SSM/I brightness temperatures and is used to calculate a *new* first-guess sea ice concentration, similar to the first iteration step. The *new* C_{FG} is proved as described above and so on. The iteration is continued until the difference between the modeled P, reflecting the *same* atmospheric conditions but *different* values of C_{FG} at each iteration step, and P calculated from the uncorrected SSM/I brightness temperatures is less than 0.001. This is usually achieved within the first ten iterations.
The accuracy of C would be close to 1 % if determined only by the difference threshold used for the minimization. But the coarser spatial resolution of the involved atmospheric data and the variability of the sea ice tie points due to varying sea ice and snow properties (see Figure 3) limits the accuracy to $\approx$ 10 %.

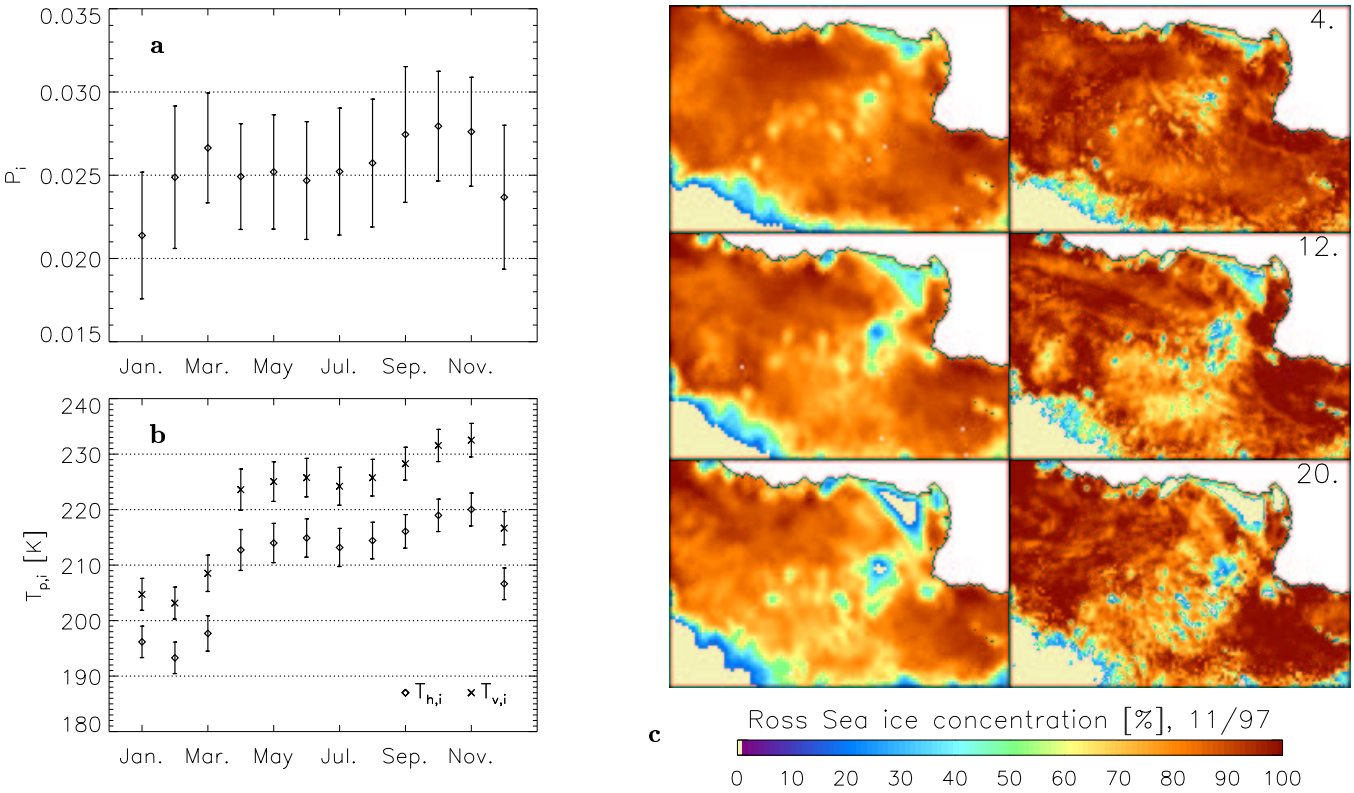

Figure 2: Left panels (a,b): Monthly 85 GHz sea ice tie points averaged over the years 1992–98: (a) P_i, (b) $T_{p,i}$. Indices h and v denote horizontal and vertical polarization. The error bars in (a) denote the sensitivity of P_i to one standard deviation of $T_{p,i}$ (error bars in (b)). Right panels (c): Evolution of the sea ice cover in the Ross Sea in November 1997: left side C_{NT}, right side C_{85}. Sea ice concentrations less than 15 % are set to zero.

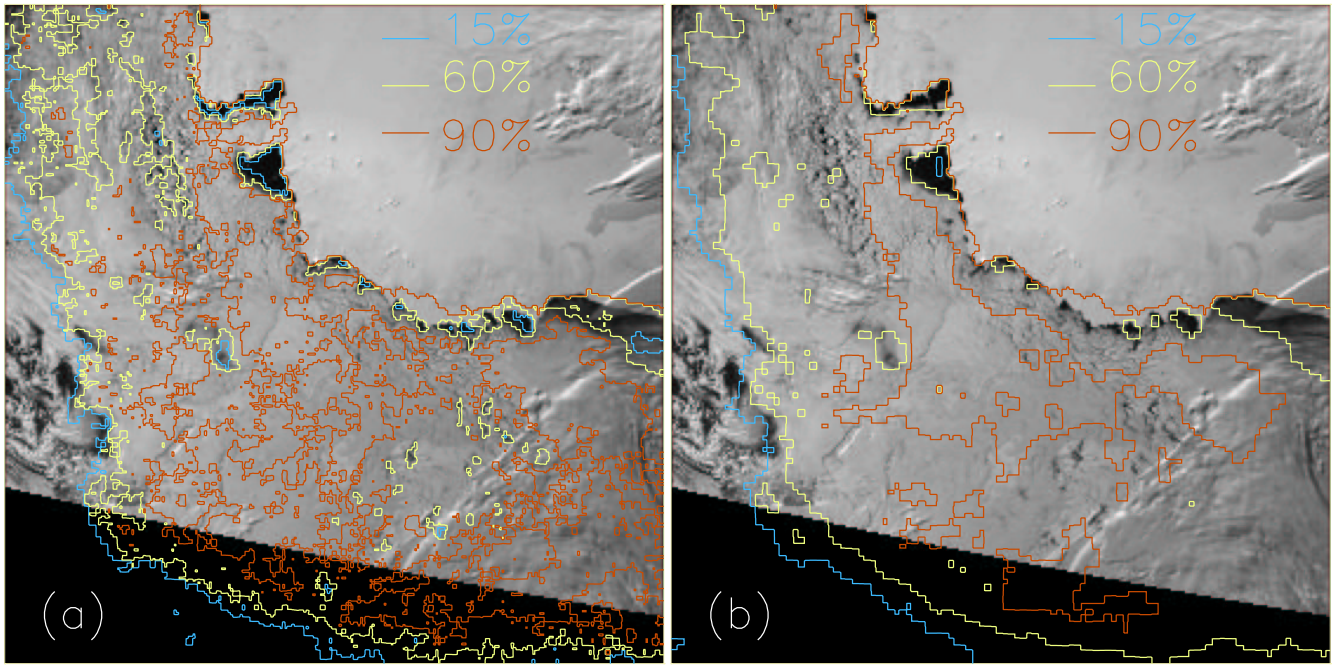

Figure 3: OLS visible images overlain with SSM/I sea ice concentration isolines of November 16, 1996: (a) C_{85}, (b) C_{NT}. The South Pole is at the upper right corner, the right (top) image borders are along 180°W (90°W).

3 Results

Figures 1a and b show monthly 85 GHz sea ice tie points averaged over the years 1992–98. The error bars in Figure 1a denote one standard deviation of P_i due to one standard deviation of $T_{p,i}$ (error bars in Figure 1b). Values of P_i vary between 0.021 (January) and 0.028 (October) and seem to decrease in summer and to increase in early winter (Figure 1a). Looking at $T_{p,i}$ (Figure 1b) freeze-up coincides well with a sharp increase of $T_{p,i}$ in March/April. The onset of melt is marked by a decrease of $T_{p,i}$ from November to January. Remarkable are the low values of $T_{h,i}$ of about 200 K in summer. This correspondes to a surface emissivity of $\approx$ 0.7 and

may be caused by old refrozen coarse grained snow. The gradually increase of $T_{p,i}$ between July and November is probably a result of a growing snow liquid water fraction, which increases ϵ_p at both polarizations (Garrity, 1992). Basing on these sea ice tie points SEA LION was used to calculate daily Antarctic sea ice concentrations C_{85} for the period 1992–98 from NSIDC daily gridded brightness temperatures. Hereafter, NASA-Team sea ice concentrations obtained with the extended weather correction (Heygster and others, 1996) are denoted by C_{NT}, Bootstrap sea ice concentrations determined with seasonal coefficients by C_{BO}.

Figure 1c shows the decay of the sea ice cover in the Ross Sea in November 1997. Much more details can be identified in the images on the right side showing C_{85} if compared to those on the left side showing C_{NT}. Figure 3 shows Operating Linescan System (OLS) visible images of the Ross/Amundsen Sea region overlain by the 15 %, 60 % and 90 % isolines of C_{85} (Figure 3a) and C_{NT} (Figure 3b) of November 16, 1996. About 16 original OLS pixels have been averaged for one OLS pixel ($\approx 10 \times 10\,\mathrm{km}^2$) shown in Figure 3. The C isolines are mapped onto the NSIDC $12.5 \times 12.5\,\mathrm{km}^2$ grid. Several coastal polynyas and a decaying sea ice cover typical for spring can be identified. The 15 % isoline of C_{NT} appears only in one polynya (Figure 3b) whereas SEA LION provides C less than 15 % in almost every polynya (Figure 3a). This seems to be quite reasonable since during November solar radiation accompanied by rising air temperatures stops the sea ice production in coastal polynyas and keeps them open (Markus and others, 1998). First polynyas within the decaying pack ice, *e. g.* in the upper left (Amundsen Sea) and the lower right quarter (Ross Sea) can be identified quite well by the 60 % and sometimes even the 15 % isoline of C_{85} (Figure 3a). There is almost no coincidence between these areas and the 60 % isoline of C_{NT} (Figure 3b).

Sea ice concentrations taken every six hours on board the research vessel *Nathaniel B. Palmer* in 1994–98 (C_{SHIP}) are compared to SSM/I sea ice concentrations ($C_{SSMI} = C_{85}$, C_{BO} or C_{NT}) mapped onto the NSIDC $25 \times 25\,\mathrm{km}^2$ grid (not shown). Daily averages of C_{SHIP} are not calculated since all observations of one day often belong to different grid cells. All values of C_{SSMI} are rounded to the nearest tenth for C_{SHIP} is given in tenths. We omit sea ice concentrations less than one tenth. Linear correlation coefficients between C_{SSMI} and C_{SHIP} vary between 0.528 (C_{85}) and 0.576 (C_{BO}). Average differences $C_{SSMI} - C_{SHIP}$ are $-5\,\%$ (C_{BO}), $-10\,\%$ (C_{85}) and $-18\,\%$ (C_{NT}). The most convincing linear regression is obtained with C_{85} (y) and C_{SHIP} (x): $y = 17.0 + 0.7 \times x$.

Daily sea ice areas and extents are calculated from C_{SSMI} for the period 1992–98 (not shown). The annual and interannual variability of SEA LION sea ice areas and extents is in line with those obtained from C_{BO} and C_{NT}. However, throughout the period SEA LION sea ice extents and areas fall below those obtained from C_{BO}. The extent difference is 0.5×10^6-$1.5 \times 10^6\,\mathrm{km}^2$. The area difference is up to $0.5 \times 10^6\,\mathrm{km}^2$ in summer and 0.5×10^6-$1.5 \times 10^6\,\mathrm{km}^2$ in winter. SEA LION sea ice extents also fall below NASA-Team sea ice extents ($\approx 1 \times 10^6\,\mathrm{km}^2$ in summer and $\approx 0.5 \times 10^6\,\mathrm{km}^2$ in winter). SEA LION sea ice areas are similar to NASA-Team sea ice areas in summer but exceed them by 0.5×10^6-$1.5 \times 10^6\,\mathrm{km}^2$ in winter.

Discussion and Conclusions

The presented iterative SEA LION algorithm uses the SSM/I 85 GHz polarization together with monthly sea ice and open water tie points, and a weather correction scheme based on radiative transfer modeling. It provides daily antarctic sea ice concentrations with a spatial resolution of $12.5 \times 12.5\,\mathrm{km}^2$. Daily sea ice extents and areas obtained from C_{85}, C_{NT} and C_{BO} agree with each other concerning the annual and interannual variability. However, SEA LION generally provides a smaller sea ice extent ($\approx 1 \times 10^6\,\mathrm{km}^2$) throughout the year. The SEA LION sea ice area is similar to those obtained from C_{NT} and C_{BO} in summer but lies between them in winter.

A comparison of Operational Linescan System (OLS) visible images with coincident isolines of C_{85} and C_{NT} shows convincing results using SEA LION, particularly concerning the areal coverage by polynyas. Sea ice concentration gradients provided by SEA LION are better resolved than those given by the NASA-Team algorithm. This may explain why the NASA-Team or Bootstrap sea ice extents are larger than the SEA LION sea ice extent (more open water pixels within the pack ice) while the NASA-Team and Bootstrap sea ice areas remain similar to the SEA LION sea ice area (smaller netto amount of sea ice covered pixels – but higher average sea ice concentration). We have compared C_{85} with 850 ship observations of the sea ice concentration (C_{SHIP}) for the period 1994–98. The results agree with those obtained with NASA-Team (C_{NT}) and Bootstrap (C_{BO}) sea ice concentrations.

The quality of the used Numerical Weather Prediction (NWP) model data, in particular the cloud liquid water content L, has a large impact on the retrieval of C_{85} and may cause large errors especially when using swath data. Further improvements of the atmospheric input parameters for the weather correction are necessary. Monthly sea ice tie points seem to consider the annual evolution of the microwave signal of almost the entire Antarctic sea ice cover but smooth out regional variations. Dividing the ice pack into zones depending on the state of snow metamorphosis and estimating regional sea ice tie points may be one step towards accounting for these variations. This point deserves further studies, in particular when looking at Figure 1b.

The upcoming Advanced Microwave Scanning Radiometer (AMSR) operates also at frequencies close to those of the SSM/I and is additionally equipped with 6 GHz channels. Its data will allow an improvement of known sea ice concentration products, mainly due to the enhanced spatial resolution of about $10 \times 10\,\mathrm{km}^2$ and probably in a more economical way since a simple weather correction seems to be sufficient. However, the AMSR will provide 89 GHz data with a higher spatial resolution than the low AMSR frequencies. These data can be used to derive higher resolved and thus more realistic

sea ice concentrations, at least under clear sky conditions.

References

Cavalieri, D.J., J.P. Crawford, M.R. Drinkwater, D.T. Eppler, L.D. Farmer, R.R. Jentz, and C.C. Wackermann. 1991. Aircraft active and passive microwave validation of the sea ice concentration from the Defense Meteorological Satellite Program Special Sensor Microwave Imager. *J. Geophys. Res.*. **96**(C12), 21,998–22,008.

Comiso, J.C., T.C. Grenfell, M. Lange, A.W. Lohanick, R.K. Moore and P. Wadhams. 1992. Microwave remote sensing of the southern ocean ice cover. In Carsey, F.D., ed. Microwave remote sensing of sea ice. AGU, Washington, D.C. 243-259.

Drinkwater, M.R. 1998. Active microwave remote sensing observations of Weddell Sea ice. In Jeffries, M.O., ed. Antarctic Sea Ice: Physical Processes, Interactions and Variability. AGU, Washington DC. 187–212.

Fuhrhop, R., G. Heygster, K.-P. Johnsen, P. Schluessel, M. Schrader and C. Simmer. 1998. A combined radiative transfer model for sea ice, open ocean, and atmosphere. *Radio Sci.*, **33**(2), 303–316.

Garrity, K. 1992. Characterization of snow on floating ice and case studies of brightness temperature change during the onset of melt. In Carsey, F.D., ed. Microwave remote sensing of sea ice. AGU, Washington, D.C. 313–328.

Grenfell, T.C., J.C. Comiso, M.A. Lange, H. Eicken and M.R. Wensnahan. 1994. Passive microwave observations of the Weddell Sea during austral winter and early spring. *J. Geophys. Res.*, **99**(C5), 9995–10,010.

Grenfell, T.C., D.G. Barber, A.K. Fung, A.J. Gow, K.C. Jezek, E.J. Knapp, S.V. Nghiem, R.G. Onstott, D.K. Perovich, C.S. Roesler, C.T. Swift and F. Tanis. 1998. Evolution of electromagnetic signatures of sea ice from initial formation to the establishment of thick first-year ice. *IEEE Trans. Geosc. Rem. Sens.*, **36**(5), 1642–1654.

Heygster, G., L.T. Pedersen, J. Turner, C.H. Thomas, T. Hunewinkel, H. Schottmue ller and T. Viehoff. 1996. PELICON: Project for estimation of long-term variability of ice concentration, *Tech. Rep.*, Contract EV5V-CT93-0268(DG12DTEE), European Community (EC).

Hollinger, J.P., R. Lo and G. Poe. 1987. Special Sensor Microwave Imager User's Guide. Naval Research Laboratory, Washington, D.C.

King, J.C. and J. Turner. 1997. Antarctic Meteorology and Climatology. Cambridge University Press. Cambridge, U.K.

Lomax, A.S., D. Lubin, and R.H. Whritner. 1995. The potential of interpreting total and multiyear-ice concentration in SSM/I 85.5 GHz imagery. *Rem. Sens. Env.*, **54**, 13–26.

Lubin, D., C. Garrity, R. Ramseier, and R.H. Whritner. 1997. Total sea ice concentration retrieval from the SSM/I 85.5 GHz channels during the Arctic summer. *Rem. Sens. Env.*, **62**, 63–76.

Markus, T., C. Kottmeier, and E. Fahrbach. 1998. Ice formation in coastal polynyas in the Weddell Sea and their impact on oceanic salinity. In Jeffries, M.O., ed. Antarctic Sea Ice: Physical Processes, Interactions and Variability. AGU, Washington DC, 273–292.

Massom, R.A., V.I. Lytle, A.P. Worby and I. Allison. 1998. Winter snow cover variability on East Antarctic sea ice. *J. Geophys. Res.*, **103**(C11), 24,837–24,855.

Maykut, G.A. 1978. Energy exchange over young sea ice in the central Arctic. *J. Geophys. Res.*, **83**(C7), 3646–3658.

Ulaby, F.T., R.K. Moore and A.K. Fung. 1981. Microwave remote sensing: active and passive. Vol. I: Microwave remote sensing fundamentals and radiometry. Artech House, Norwood, MA.

Sturm, M., K. Morris and R. Massom. 1998. The Winter snow cover of the West Antarctic pack ice: Its spatial and temporal variability. In Jeffries, M.O., ed. Antarctic Sea Ice: Physical Processes, Interactions and Variability. AGU, Washington DC. 1–18.

Svendsen, E., C. Maetzler and T.C. Grenfell. 1987. A model for retrieving total sea ice concentration from a spaceborne dual-polarized passive microwave instrument operating near 90 GHz. *Int. J. Rem. Sens.*, **8**(10), 1479–1487.

Worby, A.P. and R.A. Massom. 1995. The structure and properties of sea ice and snow cover in East Antarctic pack ice. Antarctic CRC Res. Rep. 7.